American Mineralogist, Volume 78, pages 85–95, 1993

The distribution of Ag and Sb in galena: Inclusions versus solid solution

THOMAS G. SHARP*
Department of Geology, Arizona State University, Tempe, Arizona 85287-1404, U.S.A.
PETER R. BUSECK
Departments of Geology and Chemistry, Arizona State University, Tempe, Arizona 85287-1404, U.S.A.

ABSTRACT

The distributions of Ag and Sb in galena samples from La Paz and Zacatecas, Mexico, were investigated using electron microprobe analysis, backscattered-electron imaging, and high-resolution transmission electron microscopy. Both samples contain numerous rod-shaped inclusions of diaphorite ($Pb_2Ag_3Sb_3S_8$), and the La Paz samples also contain franckeite [$(Pb,Sn)_6Sn_2Sb_2FeS_{14}$]. Although diaphorite is a common Ag-bearing inclusion in galena, franckeite has not been previously reported. Both samples have Ag concentrations nearly equal to those of Sb, indicating coupled substitution of Ag^+ and Sb^{3+} for 2 Pb^{2+}. The average $Ag_{0.5}Sb_{0.5}S$ contents of the bulk La Paz and Zacatecas samples (including inclusions) are approximately 1.37 and 0.44 mol%, respectively. Of these total $Ag_{0.5}Sb_{0.5}S$ amounts, 0.48 and 0.32 mol% occur in solid solution in galena in the La Paz and Zacatecas samples, respectively.

Inclusions of diaphorite are from 20 nm to 50 μm long, but no evidence for Ag-Sb atom clusters was found. Rod-shaped diaphorite inclusions are oriented with their **c** axes (rod axes) parallel to the ⟨100⟩ directions of galena and their **a** and **b** axes parallel to the ⟨110⟩ galena directions. The diaphorite-galena interfaces are semicoherent, with misfit dislocations every 6 to 10 nm. Disk-shaped inclusions of franckeite in the La Paz samples are oriented with their **a***, **b**, and **c** axes parallel to the ⟨100⟩ directions of galena. The top and bottom interfaces of the disks are parallel to the (100) layers of franckeite and appear to be coherent with the galena. The franckeite inclusions have a modulated-layer structure with a wavelength of 3.55 nm, which is significantly smaller than that of previously described franckeite. Both diaphorite and franckeite inclusions appear to have resulted from coherent exsolution at low temperatures. Diaphorite appears to occur metastably relative to freieslebenite ($AgPbSbS_3$), suggesting that there is a coherent solvus between diaphorite and galena.

INTRODUCTION

The distribution of precious metals in sulfide minerals is of economic, crystallographic, and geologic importance. Accurate knowledge of precious metal distributions is of economic importance for maximizing metal recovery and improving metallurgical techniques. The crystallographic significance of precious metal distributions is in understanding how "foreign" atoms are accommodated in sulfide structures and in the crystallographic controls on exsolution. Understanding the primary vs. secondary nature of precious metals, as well as the processes and conditions of ore deposition, is of significant geologic importance.

The occurrence of precious metals in sulfide minerals and their economic importance has been addressed by, among others, Cabri (1987, 1992) and Chryssoulis and Cabri (1990). Distinguishing submicroscopic inclusions from material that is structurally bound in solid solution is crucial for understanding the distributions of precious metals and the processes of their incorporation and recovery. This is particularly difficult for invisible Au, which occurs as either submicroscopic particles or in solid solution with sulfides, sulfarsenides, and arsenides. Ag occurs in more minerals than Au and is common in many base-metal minerals, either in the form of Ag-bearing inclusions or in solid solution. By overlooking Ag in such common minerals, significant amounts of Ag are lost in processing (Cabri, 1987, 1992).

Microbeam techniques are very useful for determining the concentrations and distributions of precious metals in minerals (Cabri, 1992), but such techniques cannot always distinguish precious metals in solid solution from microscopic inclusions of precious-metal-bearing minerals. If such inclusions are not accounted for in analyses, the result could be unrealistically high solid-solution estimates or incorrectly interpreted substitution mechanisms. SEM imaging of samples can be used to determine

* Present address: Bayerisches Geoinstitut, Universität Bayreuth, Postfach 10 12 51, 8580 Bayreuth, Germany.

0003–004X/93/0102–0085$02.00

the presence of microinclusions that are larger than about 100 nm, but the high spatial resolution of transmission electron microscopy (TEM) is needed to observe smaller particles. In addition, the structural relations between inclusions and the host mineral can be obtained with TEM to interpret better the origins of inclusions. High-resolution transmission electron microscopy (HRTEM) has recently been applied to the problem of invisible Au in arsenopyrite (Cabri et al., 1989) and disseminated Au in Carlin-type deposits (Bakken et al., 1989). In the first case (Cabri et al., 1989), Au particles were not observed, suggesting that the Au is structurally bound, whereas Bakken et al. (1989) found Au particles less than 20 nm in diameter that had not been previously observed.

High-sensitivity analytical techniques, such as proton-induced X-ray emission (Cabri, 1987; Cabri et al., 1984, 1985) and secondary-ion mass spectrometry (McIntyre et al., 1984; Chryssoulis et al., 1986; Chryssoulis and Cabri, 1990; Cabri et al., 1989, 1991), combined with careful inspection for inclusions, have been used to show that trace concentrations of precious metals occur in many sulfide minerals. Samples of galena containing relatively high concentrations of Ag, Bi, and Sb have been studied using electron-microprobe analysis (EMPA) (Laflamme and Cabri, 1986a, 1986b; Foord et al., 1988), but HRTEM (Sharp and Buseck, 1989) and scanning tunneling microscopy (STM) (Sharp et al., 1990) have only recently been applied to Ag-bearing galenas.

Concentrations of Ag in galena are variable and depend on the presence of other elements such as Sb and Bi. The simple substitution of Ag for Pb ($2Ag^{+} = Pb^{2+}$) is limited to a maximum of 0.4 mol% Ag_2S at 700 °C and less at lower temperatures because half of the Ag must go into interstitial sites (Van Hook, 1960; Karup-Møller, 1977). Where Ag^{+} substitution for Pb^{2+} is coupled with substitution of Sb^{3+} or Bi^{3+} [$Ag^{+} + (Sb,Bi)^{3+} = 2Pb^{2+}$], the charge and cation-anion ratio are balanced, allowing higher Ag concentrations. Galena with combined Ag, Sb, and Bi concentrations greater than 0.5 wt% is called galena solid solution by Foord et al. (1988), who report samples containing as much as 9.4 and 18.5 wt% Ag and Bi, respectively. Whereas excess Ag relative to Sb or Bi is limited by interstitial substitution of Ag, excess Sb or Bi is more easily accommodated by the substitution mechanism $2(Sb, Bi)^{3+} + \square = 3Pb^{2+}$), resulting in vacancies on Pb sites. The lattice constants for the $AgSbS_2$-galena solid solution show a negative deviation from ideality, which is interpreted as evidence for clustering of the solute atoms in the solid solution (Wernick, 1960; Godovikov and Nenasheva, 1968).

Galena solid solution and the sulfosalt inclusions may be useful as indicators of depositional conditions. The coexistence of galena, galena solid solution, and a variety of sulfosalts was interpreted as evidence for multiple stages of mineralization in the Round Mountain and Manhattan Au districts, Nevada (Foord et al., 1988). Experimentally determined phase relations in the Ag_2S-Sb_2S_3-PbS system indicate a solvus between freieslebenite ($AgPbSbS_3$) and galena solid solution below 420 to 390 °C (Hoda and Chang, 1975; Amcoff, 1976) that may be useful as an indicator of deposition temperatures. However, our results, as well as previous studies (Czamanske and Hall, 1976; Laflamme and Cabri, 1986a, 1986b), suggest that diaphorite ($Pb_2Ag_3Sb_3S_8$), rather than freieslebenite, is the major inclusion type in Ag- and Sb-bearing galena.

The purpose of the present study is to investigate the distribution of Ag and Sb between solid solution and inclusions in galena samples from two Ag deposits. The compositions of the galena and inclusions are determined with EMPA. The type and size distribution of the inclusions are determined with TEM, as are the structural relations to the host galena. The origins of the inclusions are discussed in terms of their morphologies and crystallographic relations to galena.

Samples and characterization techniques

The Ag- and Sb-bearing galena samples used in this study were from the La Paz and Zacatecas Ag districts, Mexico. Most published studies of Ag-bearing galena have focused on coupled substitution of Ag with Bi; for this study samples were chosen that contain up to 1 wt% Ag and Sb, with no detectable Bi and only trace amounts of As, Sn, and Te. Both samples contain Ag-Sb inclusions, predominantly diaphorite, and minor amounts of other sulfosalts. These galena samples were also chosen for their large crystal size, which was required for previously reported STM investigations (Sharp et al., 1990).

In addition to the Ag- and Sb-bearing samples, Ag-free galena (from an unknown location) and synthetic Ag-bearing and Sb-Bi-free galena (provided by Louis Cabri) were examined. These samples were used as controls to determine whether observed defects correlate with Ag and Sb concentrations.

Chemical analyses were obtained with a Jeol JXA 8600 Superprobe electron microprobe using an accelerating potential of 15 kV. Cleavage fragments of galena were mounted in epoxy resin, polished, and C coated, resulting in polished surfaces nearly parallel to (100) planes. Backscattered-electron imaging (BEI) was used to locate sulfosalt inclusions and to observe their textural relations to the galena host. Inclusions and the galena host were analyzed with wavelength-dispersive X-ray spectroscopy for Pb, S, Ag, Sb, Bi, As, and Sn, using common sulfides and Bi metal as standards. The galena host (between inclusions), was analyzed using a 50-nA beam current to obtain high count rates for Ag and Sb. Based on 1σ counting statistics, the precision of these analyses is ± 0.02 wt%. Analyses of the host galena plus inclusions were obtained by rastering the beam over areas 120×120 μm. Because the rastered-beam analyses and those of the micrometer-sized inclusions have contributions from inclusions and matrix, the results are only semiquantitative.

For HRTEM studies, cleaved slabs of galena were glued to 3-mm Cu grids, mechanically thinned to approximately 50 μm, and ion milled with 5-kV Ar ions until

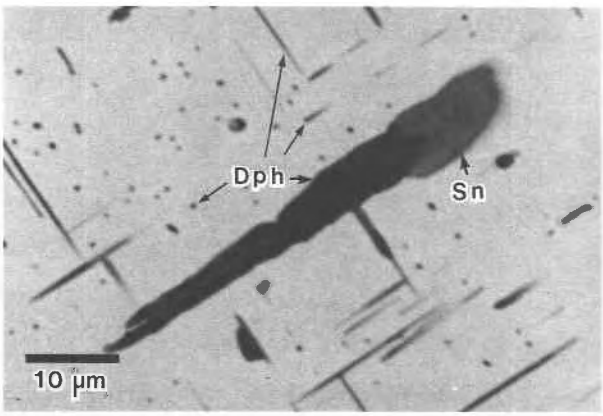

Fig. 1. A backscattered-electron image of La Paz galena with diaphorite (Dph) and Sn-bearing (Sn) inclusions. A large, irregularly shaped diaphorite grain, as well as the typical rod-shaped inclusions, are indicated. The orientation of the diaphorite rods along the galena ⟨100⟩ directions produces the dark orthogonal lines and spots depicted here. An example of the Sn-bearing material occurs at the end of the large diaphorite grain.

the slabs were perforated. Low-voltage milling (1.6 kV) was done to remove excess bombardment-damaged material. Electrical contact between the samples and the Cu grids was achieved by either applying a light C coat or by making a bridge with conductive C paint. Crushed samples, suspended on holey-carbon grids, were examined to monitor ion-bombardment damage in the milled samples.

HRTEM experiments were conducted with a Jeol 2000FX using an accelerating potential of 200 kV. Imaging and selected-area electron diffraction experiments (SAED) were done along the ⟨100⟩ axes of galena. SAED was used to identify inclusions and to determine their orientation and crystallographic relations to host galena. Structural and interfacial relations with galena were determined by HRTEM imaging of the inclusions and their boundaries.

Ag-Sb distribution between galena and inclusions

Although the Ag- and Sb-bearing inclusions in these samples are not visible by reflected-light microscopy, they stand out in high-magnification and high-contrast BEI micrographs. The predominant inclusions in both samples are diaphorite, which appear as dark linear features and nearly round spots (Fig. 1). This texture suggests that the inclusions are orthogonally oriented rods within the galena. Most rods appear to be 0.5 to 2.0 μm in diameter and as long as 50 μm, although larger and less regularly shaped diaphorite inclusions occur in the La Paz sample. Diaphorite inclusions of similar size and shape also occur in galena from the Brunswick 12 mine (Laflamme and Cabri, 1986a, 1986b).

In addition to diaphorite, the La Paz sample contains significant amounts of Sn-bearing inclusions. These inclusions appear in BEI micrographs (Fig. 1) as irregularly shaped grains that are commonly associated with diaphorite. Many display variable contrast in such images, indicating chemical heterogeneity and possibly a multiphase character. The Sn-bearing inclusions seen with BEI were not observed with HRTEM, but the Sn-Ag-Sb mineral, franckeite, was commonly encountered in the La Paz sample with HRTEM. Additional inclusions such as boulangerite ($Pb_5Sb_4S_{11}$) and some Ag-rich tellurides were observed in the La Paz and Zacatecas samples, but they are rare.

Electron microprobe analysis (EMPA) of the inclusions is limited by their small sizes; many analyses of the diaphorite inclusions have excess Pb, indicating that even for the larger inclusions there can be contributions from the surrounding galena. The compositions of diaphorite, Sn-bearing inclusions, and boulangerite are presented in Table 1, together with the stoichiometric compositions

Table 1. Electron microprobe data for inclusions in La Paz galena and Ag and Sb contents of La Paz and Zacatecas galena (± inclusions)

							La Paz		Zacatecas	
	Diaphorite [6]	Ideal diaphorite	Sn phase [3]	Ideal Pb-franckeite	Boulang. [1]	Ideal boulang.	Galena [21]	+ inclusions [12]	Galena [24]	+ inclusions [12]
S	18.95(0.30)	18.86	16.44(2.0)	21.88	18.13	18.80				
Ag	22.92(0.53)	23.80	8.44(10)		0.02		0.22(0.12)	0.62(0.06)	0.14(0.08)	0.19(0.07)
Sb	26.55(0.41)	26.86	15.51(12)	11.87	25.24	25.96	0.28(0.14)	0.81(0.06)	0.19(0.09)	0.27(0.06)
Pb	30.86(0.73)	30.48	59.90(21)	40.39	55.57	55.23				
Sn			1.13(0.84)	23.14	0.32					
Fe				2.72						
Total	99.28(0.60)	100.00	101.42(2.0)	100.00	99.28	99.99				
	Inclusion stoichiometry based on given no. of S atoms and at% Ag and Sb									
S	8.00	8.00	14.00	14.00	11.00	11.00				
Ag	2.88	3.00	1.98				0.24(0.13)	0.69(0.07)	0.16(0.09)	0.22(0.08)
Sb	2.95	3.00	3.28	2.00	4.03	4.00	0.27(0.13)	0.79(0.06)	0.18(0.09)	0.27(0.06)
Pb	2.02	2.00	8.21	4.00	5.22	5.00				
Sn			0.27	4.00	0.05					
Fe				1.00						
Total	15.85	16.00	27.74	25.00	19.30	19.00				

Note: The numbers in brackets correspond to the number of analyses presented, whereas the numbers in parentheses correspond to the standard deviations of the data.

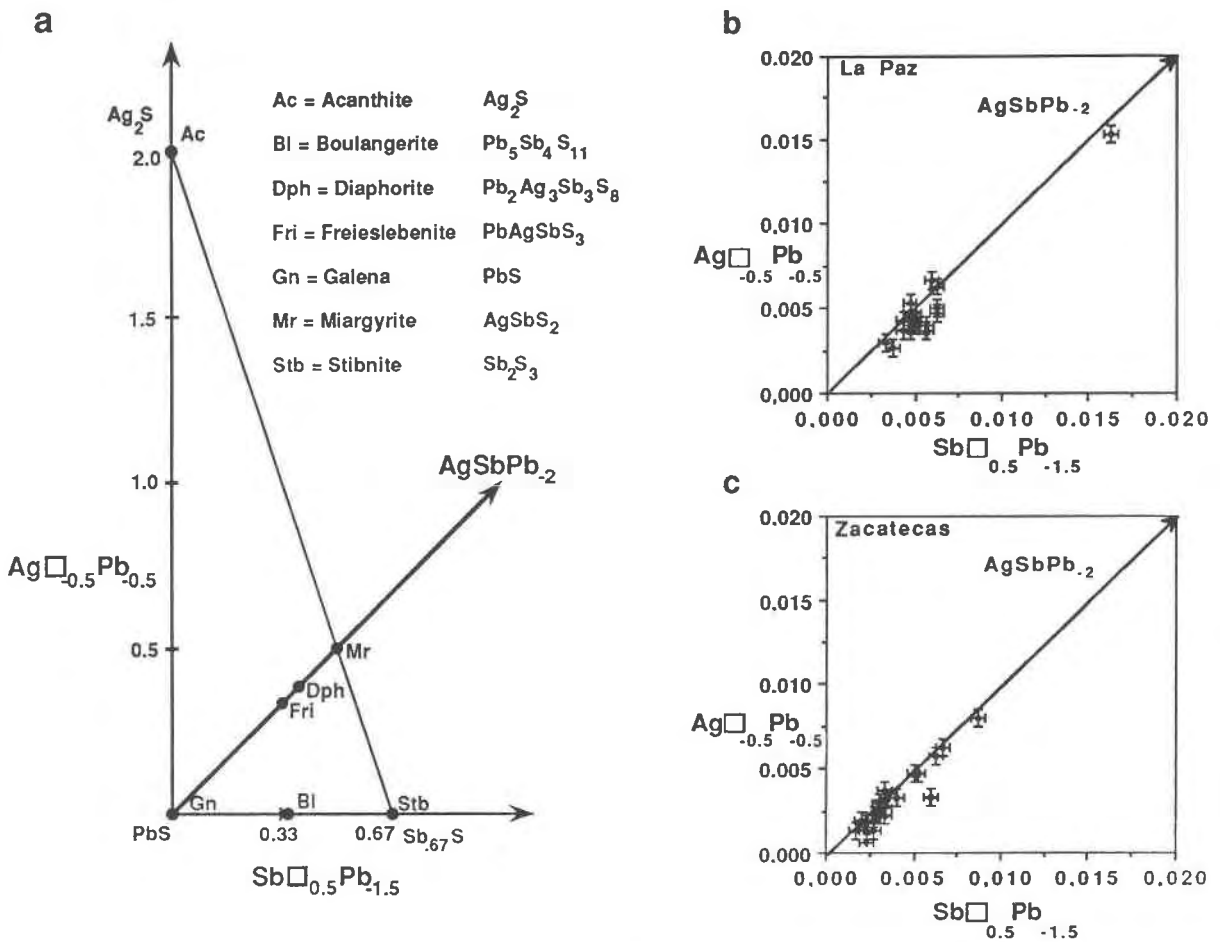

Fig. 2. Chemographic and substitution relations (**a**) in the Ag_2S-PbS-$Sb_{0.67}S$ system showing substitution vectors relating galena to acanthite, stibnite, miargyrite, boulangerite, freieslebenite, and diaphorite. The PbS corner of the triangle is enlarged to show the substitutions of Ag and Sb in the (**b**) La Paz and (**c**) Zacatecas samples. Many data plot along or slightly below the $AgSbPb_{-2}$ coupled-substitution vector.

of these minerals and Pb-rich franckeite for comparison. The analyses of diaphorite and boulangerite are near their stoichiometric compositions, but that of the Sn-bearing materials does not closely resemble franckeite. The Sn-bearing inclusions contain high concentrations of Ag and Sb and little Sn relative to franckeite and may represent a mixture of minerals.

The Ag and Sb concentrations were quite variable, reflecting the distribution of dissolved Ag and Sb, as well as inclusions too small to be resolved with BEI, and average values are presented in Table 1. Concentrations of Ag ranged from 0.11 to 0.69 wt% (mean = 0.22 ± 0.12 wt%) for the La Paz sample and from 0.04 to 0.36 wt% (mean = 0.14 ± 0.08 wt%) for the Zacatecas sample. The Sb concentrations range from 0.18 to 0.84 wt% (mean = 0.28 ± 0.14 wt%) for the La Paz sample and from 0.08 to 0.45 wt% (mean = 0.19 ± 0.09 wt%) for the Zacatecas sample.

The mechanisms of Ag and Sb substitution are examined by plotting the concentrations in terms of substitution vectors $Ag\square_{-0.5}Pb_{-0.5}$ and $Sb\square_{0.5}Pb_{-1.5}$ (Fig. 2). The chemographic and substitution relations among galena, stibnite, acanthite, miargyrite, diaphorite, and freieslebenite are illustrated (Fig. 2a), with the right triangle defined by the components Ag_2S, PbS, and $Sb_{0.67}S$, (normalized to one S atom). In this diagram, application of the $Ag\square_{-0.5}Pb_{-0.5}$ vector two times transforms PbS into Ag_2S (acanthite) and application of the $Sb\square_{0.5}Pb_{-1.5}$ vector 0.67 times transforms PbS into $Sb_{0.67}S$ (stibnite). The galena corner of this triangle is enlarged in Figures 2b and 2c to illustrate the correlation between Ag and Sb substitutions in the galena solid solution. The Ag and Sb substitution (y and x, respectively) are calculated from the atom percents using the general formula $Pb_{1-1.5x-0.5y}Ag_ySb_xS$ for the Ag_2S-PbS-$Sb_{0.67}S$ system. Because the cation-anion ratios change in this system, except along the coupled-substitution vector, the substitution is not linearly related to the atom percent. However, at the low Ag and Sb contents of these samples, the substitution is approximately two times the Ag and Sb atom percent. As

Table 2. Dimensional relations among galena, diaphorite, freieslebenite, and franckeite

Mineral	Space Gp.	Unit cell (nm)			Subcell*			% misfit relative to galena		
		a	*b*	*c*	β	a_s	b_s	*a*	*b*	*c*
Galena (1)	$F4/m\bar{3}2/m$	0.594	0.594	0.594	90°	$a\sqrt{2}/2$	$a\sqrt{2}/2$			
Diaph. (2)	$C2_1/a$	1.584	3.208	0.590	90°10′	*a*/4*	*b*/8*	−5.7**	−4.5**	−0.5†
Freies. (3)	$P2_1/n$	0.753	1.279	0.588	92°14′	*a*/2*	*b*/3*	−10.4**	1.4**	−1.0†
Frnk. T (4)		1.72	0.579	0.581					−2.5†	−2.0†
Frnk. H (4)		1.72	0.365	0.63					−38.6†	6.7†

Note: Crystallographic data from (1) Wycoff, 1963, (2) Hellner, 1957a, (3) Hellner, 1957b, and (4) Williams and Hyde, 1988.
* Subcell shown in Figure 3.
** Misfit relative to galena d_{110}.
† Misfit relative to galena d_{100}.

can be seen in Figure 2, Ag vs. Sb substitutions for both samples plot along but slightly below the $AgSbPb_{-2}$ vector, indicating coupled substitution with a slight excess of Sb relative to Ag, presumably accompanied by vacancies on Pb sites.

The results of the rastered-beam analyses (galena plus inclusions, Table 1) indicate that the total Ag and Sb concentrations in the La Paz sample are approximately 0.62 (±0.06) and 0.81 (±0.06) wt%, respectively, whereas the total Ag and Sb concentrations in the Zacatecas sample are approximately 0.19 (±0.07) and 0.27 (±0.06) wt%, respectively. The distribution of Ag and Sb between galena and inclusions can be estimated by subtracting the $Ag_{0.5}Sb_{0.5}S$ contents of the galena from those determined by rastered-beam analyses. In the La Paz sample, the total $Ag_{0.5}Sb_{0.5}S$ content is 1.37 mol%, with 0.48 mol% in the solid solution and 0.89 mol% as inclusions, principally diaphorite. The total $Ag_{0.5}Sb_{0.5}S$ content of the Zacatecas sample is 0.44 mol%, with 0.32 mol% in solid solution, leaving only 0.12 mol% $Ag_{0.5}Sb_{0.5}S$ to account for diaphorite inclusions.

Structural relations between galena and inclusions

The structures of galena, diaphorite, and freieslebenite are closely related, allowing coherent intergrowth and interface relations such as those observed in HRTEM images. Unit-cell and subcell relations among these minerals are summarized in Table 2 and illustrated in Figure 3. Galena has the NaCl structure, with octahedrally coordinated Pb and S defining a face-centered cubic lattice. The structures of diaphorite and freieslebenite are derivatives of galena, with the same octahedral arrangement of cations and S anions, but with Ag^+ and Sb^{3+} substituted for Pb^{2+}. Both diaphorite and freieslebenite have galena-like subcells (Hellner, 1957a, 1957b), as illustrated in Figure 3. The presence of Sb^{3+} (radius 0.89 nm; Shannon, 1976), which is considerably smaller than Pb^{2+} (radius 1.33 nm), results in the diaphorite subcell parameters ($a_s = a/4$, $b_s = b/8$, and $c_s = c$) somewhat smaller than $a_g\sqrt{2}/2$, and a_g of galena. The freieslebenite subcell ($a_s = a/2$, $b_s = b/3$, and $c_s = c$) is also smaller than the primitive galena subcell, but with most of the misfit along the freieslebenite **a** axis.

Franckeite $[(PbSn)_6Sn_2Sb_2FeS_{14}]$ is a layered mineral consisting of alternating (along **a**) pseudotetragonal (T) and pseudohexagonal (H) sheets that have an incommensurate relation (Makovicky, 1974, 1976; Moh, 1984, 1987; Williams and Hyde, 1988; Wang and Kuo, 1991). The T-sheet structure is either PbS-like or slightly sheared, making it SnS-like, with Sb^{3+} and Ag^+ substituting for Pb^{2+} or Sn^{2+}; its thickness is approximately 1.2 nm along **a**. The cell parameters that are parallel to the sheet, b_T = 0.579 and c_T = 0.581 nm (Williams and Hyde, 1988), are

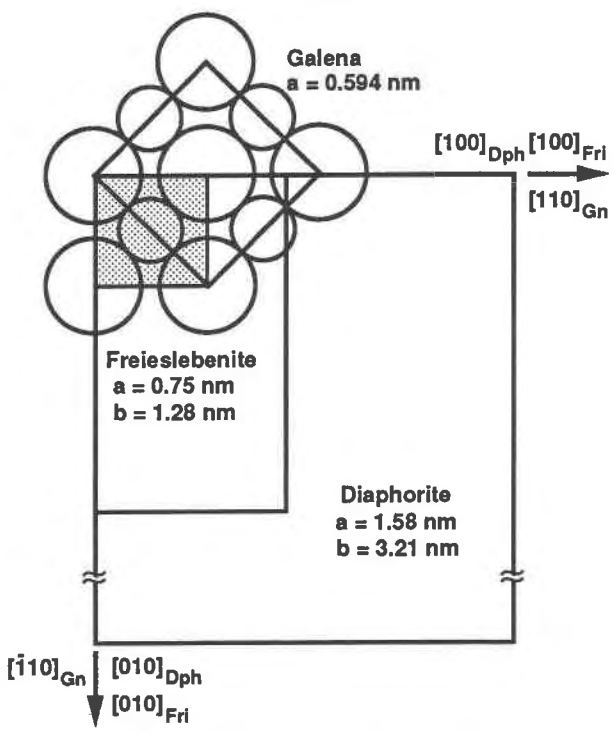

Fig. 3. Schematic illustration of the unit-cell relations among galena, diaphorite, and freieslebenite as viewed along their **c** axes. The box illustrating the diaphorite unit cell is truncated to save space. The cation (small circles) and anion (large circles) arrangement and the subcell (shaded box) common to all three structures are illustrated. The galena face diagonal, along [110], is significantly longer than the freieslebenite *a* parameter, illustrating the large misfit between these minerals along **a**.

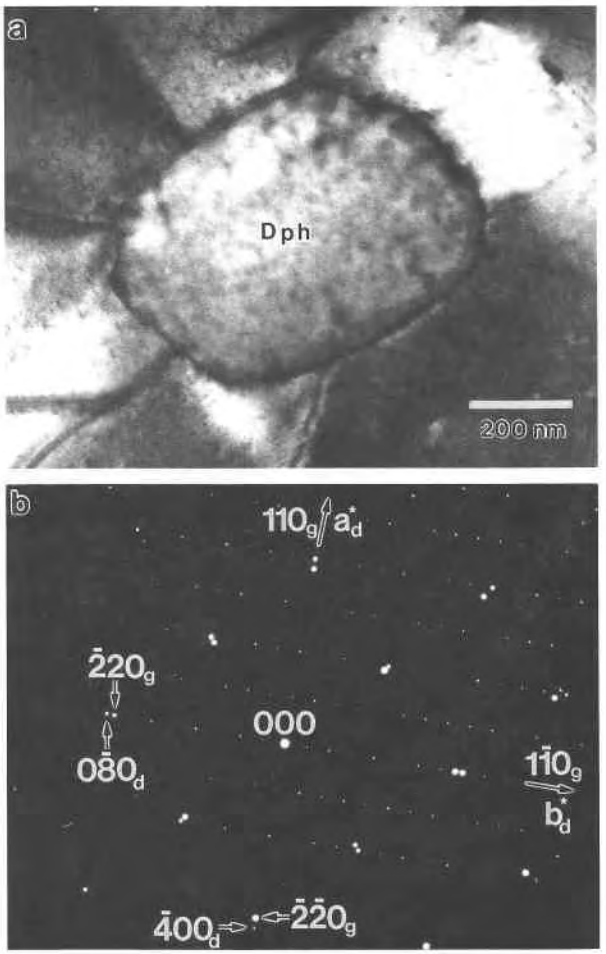

Fig. 4. (**a**) TEM image of a diaphorite rod viewed along the rod axis and (**b**) the corresponding SAED pattern. The trace of the diaphorite-galena interface and dislocations extending from the interface appear as dark lines in the image. The interface has flattened sides that are subparallel to the {120} planes of diaphorite and {100} planes of galena. The SAED pattern along the diaphorite and galena [001] zone axes illustrates that the **a*** and **b*** directions of diaphorite are parallel to the ⟨110⟩ directions of galena. The intense substructure reflections of diaphorite $\bar{4}00$ and $0\bar{8}0$ are nearly coincident with the $\bar{2}20$ and $\bar{2}20$ reflections of galena.

only slightly smaller than the galena cell parameter a_g and can fit well into the galena structure. The H sheet is a derivative of the berndite (SnS_2) structure, with Fe^{3+} substituted for Sn^{4+}; it is approximately 0.5 nm thick, with cell parameters $b_H = 0.365$ nm and $c_H = 0.63$ nm parallel to the sheet (Williams and Hyde, 1988). The large misfit between the H and T sheets results in the incommensurate structure. An alternating sequence of the T and H sheets produces a layered structure 1.72 nm thick, with a sinusoidal modulation along **c*** and with a variable wavelength of 4.2 nm (Williams and Hyde, 1988) to 4.7 nm (Wang and Kuo, 1991).

HRTEM OBSERVATIONS

Diaphorite inclusions

Diaphorite inclusions are abundant in both the La Paz and Zacatecas samples. Most are rod shaped, with the rod axis parallel to the diaphorite **c** axis; many are nearly round, but some have partial {120} faces (Fig. 4a) or irregular shapes. Diaphorite rods in the La Paz sample are commonly 300–600 nm in diameter, and those in the Zacatecas sample 100–200 nm, but inclusions as large as several micrometers in diameter and as small as 20 × 200 nm have been observed. The smallest of these inclusions are not visible by BEI and would therefore be incorporated into analyses of the solid solution. The rare occurrence of these inclusions on the scale of 20–200 nm suggests that galena analyses reflect primarily Ag and Sb in true solid solution.

The orientation relation suggested by the textures in BEI micrographs is confirmed by TEM observations. Diaphorite rods (c axis = rod axis) are parallel to the three ⟨100⟩ directions in galena. This relation is a result of the almost identical values of the *c* cell parameter of diaphorite (0.590 nm) and *a* cell parameter of galena (0.594 nm). SAED patterns of the diaphorite [001] and the galena [001] zone axes (Fig. 4b) show that the **a*** and **b*** directions of diaphorite are parallel to the ⟨110⟩* directions of galena. The substructure of diaphorite is indicated in the [001] SAED pattern (Fig. 4b) by high-intensity reflections that occur very near the galena reflections. The NaCl arrangement of cations and anions in diaphorite results in a substructure diffraction pattern that is essentially the same as that of galena. The diaphorite $\bar{4}00$ and $0\bar{8}0$ diffraction spots are examples of subcell reflections that are located adjacent to the corresponding galena reflections, indicative of a diaphorite subcell that is somewhat smaller than that of galena.

Diaphorite-galena interfaces

The interfaces between diaphorite and galena are semicoherent, with periodic steps (Fig. 5a) and misfit dislocations (Fig. 5b). Because of the smaller diaphorite subcell, a semicoherent relation requires extra atomic planes on the diaphorite side of the boundary. The terminations of these layers at the boundary resemble dislocations and can be described in terms of Burgers vectors and circuits. Burgers circuits drawn around misfit dislocations (Fig. 5b) indicate extra (240) and ($2\bar{4}0$) atomic planes in diaphorite analogous to the {200} planes of galena. The corresponding Burgers vectors are 0.28 nm along diaphorite [110] or [$1\bar{1}0$], where only one extra atomic plane occurs, and 0.40 nm along [100] or [010], where two orthogonal extra planes occur together. In Figure 5b, the Burgers circuit on the left side of the figure reveals only one extra atomic plane, whereas the circuits in the center and on the right side show two extra planes. A single extra atomic plane (0.28-nm Burgers vector) would result in anions on cation sites (Fig. 6) and a charged stacking fault, which would be highly unlikely in a galena-like structure. The

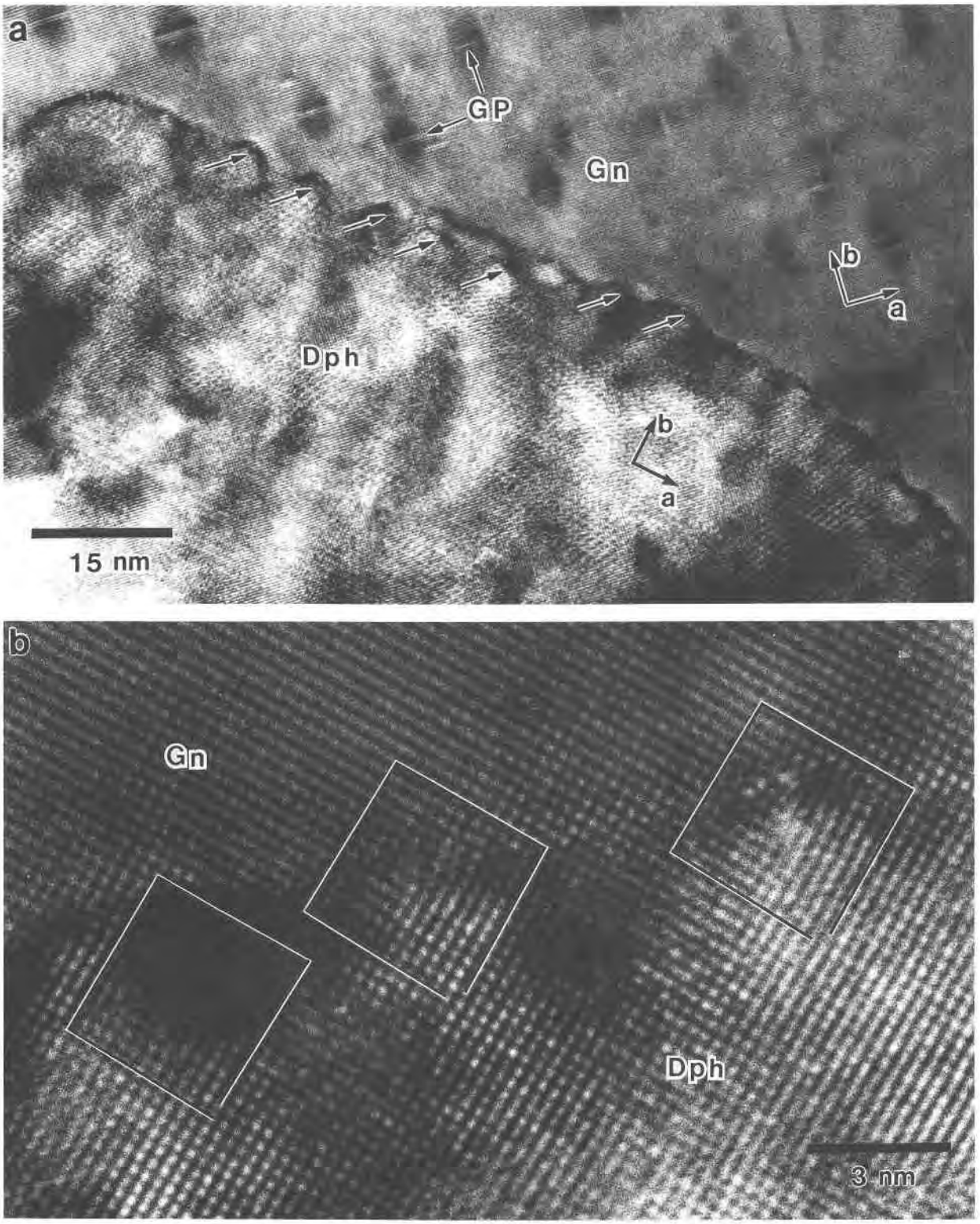

Fig. 5. HRTEM images of a diaphorite (Dph) inclusion in galena (Gn), viewed along [001], illustrating the structure and morphology of the diaphorite-galena interface. The orientation relationship (**a**) is illustrated by the **a** and **b** lattice vectors of both minerals. The interface is curved with facets (at arrows) parallel to the {100} planes of galena. A higher magnification image (**b**) of this interface shows misfit dislocations illustrated by the Burgers circuits (boxes). The gaps at the bottoms of the Burgers circuits represent projected Burgers vectors of ½**a**[100] (0.28 nm) and $(\sqrt{2}/2)$**a**[110] (0.40 nm) relative to the galena structure.

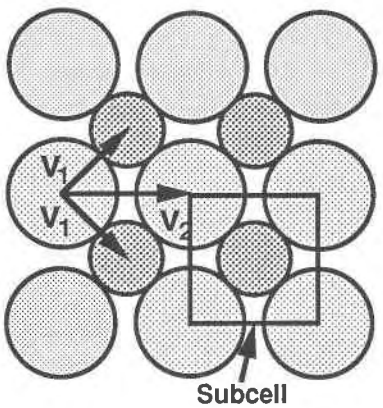

Fig. 6. Schematic illustration of the apparent Burgers vectors for the misfit dislocations observed at the galena-diaphorite interface of Fig. 5. The small dark circles correspond to the cations, the lightly shaded circles correspond to the anions, and the box indicates the subcell. The $\mathbf{v}_1$ Burgers vectors, along the galena ⟨100⟩ directions, are unlikely because they connect anion to cation sites. The $\mathbf{v}_2$ vector, along the galena [110] direction, is 0.40 nm long and connects equivalent ion sites.

apparent 0.28-nm dislocation probably has an equivalent 0.28-nm screw component along **c** that is invisible in this projection. If this model is correct, all the misfit dislocations are equivalent to the 0.40-nm type, but with some accommodating misfit along **c** as well as along **a** or **b**.

The spacings of the misfit dislocations are consistent with the values expected from the calculated misfit between diaphorite and galena. Dislocations with Burgers vectors of 0.40 nm along **a** on a diaphorite (010) boundary would accommodate the 5.7% misfit if spaced every 7.0 nm along **a**. The distance between the two dislocations with 0.40-nm Burgers vectors in Figure 5b is 7.8 nm. The separation expected between a 0.28-nm dislocation and a 0.40-nm dislocation is 5.3 nm, as compared with the 5.6-nm value observed in Figure 5b. On a larger scale (Fig. 5a), the diaphorite (010) boundary consists of small {110} facets that are associated with misfit dislocations. The spacing of these facets is 6.3–8.3 nm, which is comparable to the distance between dislocations with 0.40-nm Burgers vectors.

Franckeite inclusions

In addition to diaphorite, franckeite has been observed in the La Paz sample (Fig. 7). These inclusions have disk-like morphologies parallel to their (100) layers. The disks are 60–150 nm thick and occur parallel to the galena {100} planes. In the HRTEM images of franckeite inclusions viewed along [010] (Figs. 7a, 8a), the 1.72-nm layers and their sinusoidal modulations are clearly visible. The SAED pattern for this orientation (Fig. 7b) suggests a topotaxial relation between galena and franckeite, where **b**, **a***, and **c*** of franckeite are nearly parallel to the ⟨100⟩ directions of galena and the T-sheet structure nearly matches that of galena. The fact that the T-sheet diffraction rows along **a*** coincide with the galena reflections indicates nearly identical atomic spacings in the two structures. Streaking along **a*** in the T-sheet rows indicates a stacking disorder of the sheets.

The closely spaced reflections along the modulation vector **q** (crossing the rows of T-sheet reflections) correspond to a 3.55-nm modulation of the T sheets. This 3.55-nm wavelength is considerably smaller than the 4.2–4.7 values reported for franckeite (Williams and Hyde, 1988; Wang and Kuo, 1991) and may be a result of high Ag and Sb contents. Although Ag^+, Sn^{2+} and Pb^{2+} all have comparable ionic radii in sixfold coordination (≈0.130 nm), the radius of Sb^{3+} is only 0.089 nm (Shannon, 1976). Excess substitution of Sb^{3+} (and thus Ag^+) for Pb^{2+} and Sn^{2+} in the pseudotetragonal sheet of franckeite would increase the misfit between T and H sheets, requiring a greater modulation of the structure.

The layers of franckeite are further resolved into their T and H sheets in Figure 8. The images show offsets of the lattice fringes across both sheets, indicating sheared structures. The problem of the PbS-like vs. SnS-like structure of the T sheet was investigated by Williams and Hyde (1988), who presented image calculations that can be used to distinguish between the PbS- and SnS-like structures. Their image simulations indicate fringes normal to the T layers for the PbS-type structure and fringes oblique to the T layers for the SnS-type structure. The image presented here (Fig. 8a) resolves the lattice fringes in the T sheet, showing that they are oblique to the sheets, similar to the image calculations of the SnS-like structure presented by Williams and Hyde (1988).

Franckeite-galena interfaces

The franckeite inclusions are coherently intergrown with galena. The most extensive of the boundaries is parallel to the franckeite (100) layers and the galena (100) planes. Here the (020) lattice fringes of galena are continuous into the franckeite, with minor offsets but with no apparent misfit dislocations (Fig. 8). This observation implies that a small amount of misfit at the interface is accommodated by homogeneous strain. An interesting form of interfacial strain is evident in franckeite inclusions that are imaged along [010] (Fig. 8a), where the amplitude of the modulations decreases toward the (100) boundary. Such a flattening of the modulation apparently results in a better fit between the H sheet of franckeite and the galena at the interface. A step is present along the boundary in Figure 8a, where a 1.7-nm layer of franckeite terminates into the galena. The step is evident as the termination of an H sheet, but with a smooth transition from the galena to the T sheet below the terminated H sheet. The presence of such steps at these interfaces suggests a layer-by-layer growth mechanism for the franckeite inclusions.

Defects in galena

Defects that resemble Guinier-Preston (G-P) zones (Fig. 5a) are abundant in ion-milled galena, but are absent in all of the crushed samples, suggesting that they are artifacts of ion thinning.

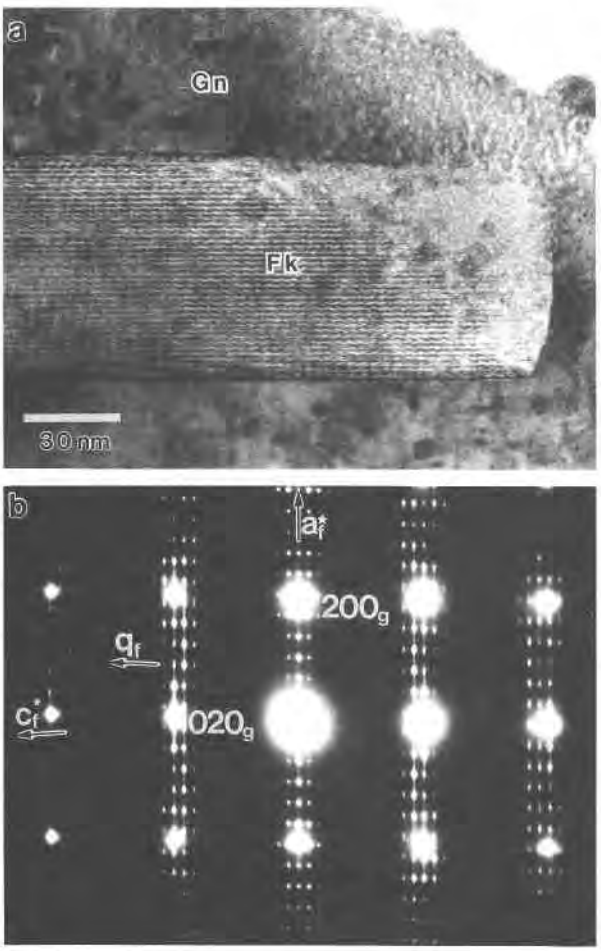

Fig. 7. (**a**) TEM image of a franckeite (Fk) inclusion in galena (Gn) and (**b**) the corresponding SAED pattern. The image shows the end of a plate-shaped inclusion of franckeite viewed along the [010] zone axis. Fringes that are visible in this inclusion correspond to the 1.7-nm layers along **a** and their 3.55-nm modulations. The SAED pattern is a superposition of the franckeite [010] and galena [001] patterns. The $\mathbf{a}_f^*$ and $\mathbf{c}_f^*$ directions and the modulation vector $\mathbf{q}_f$ of franckeite are nearly parallel to the ⟨100⟩ directions of galena. The streaks along franckeite $\mathbf{a}_f^*$ indicate layer-stacking disorder.

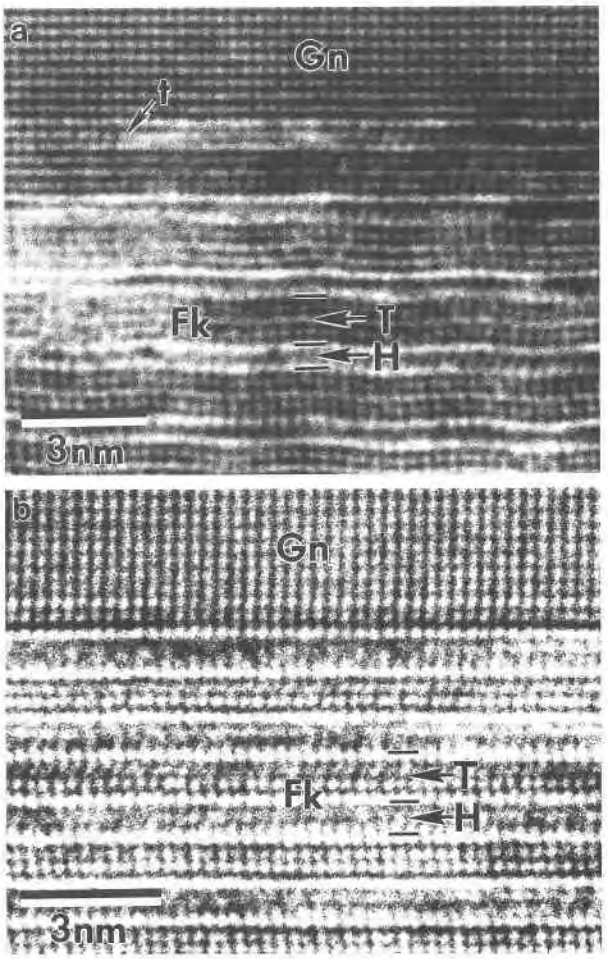

Fig. 8. HRTEM images of interfaces between galena (Gn) and franckeite (Fk) viewed along the franckeite (**a**) [010] and (**b**) [001] zone axes. In both images the pseudotetragonal (T) and pseudohexagonal (H) sheets of franckeite are resolved; the H sheets appear smeared and perhaps beam damaged and the T sheets appear galena-like but slightly sheared. The galena-franckeite interfaces are coherent with no apparent misfit dislocations, although there is some distortion of the galena (020) fringes at the interfaces and a decrease (**a**) in the modulation amplitude of the franckeite layers. A step along the interface (**a**) is evident as a termination (t) of an H sheet.

Discussion

Ag and Sb are distributed between galena solid-solution and microscopic inclusions, most of which are diaphorite, in proportions dictated by bulk concentrations and the extent of exsolution. Microscopic inclusions of diaphorite may be common in Ag-Sb-bearing galena but overlooked because of their small size and optical similarities to galena. Most diaphorite inclusions that we have observed are rods less than 1 μm in diameter, but larger diaphorite inclusions have been reported by Laflamme and Cabri (1986a, 1986b) and Czamanske and Hall (1976). Although the optical properties of diaphorite are similar to those of galena (Ramdohr, 1980), they are easily observed using BEI with high magnification and contrast. We have seen no evidence of inclusions or atom clusters smaller than 20 nm in the HRTEM results, but STM experiments on cleavage surfaces have shown distorted structure that may be a result of AgSb clusters (Sharp et al., 1990).

The rodlike morphology, orthogonal orientation, and homogeneous distribution of the diaphorite inclusions are strong evidence for exsolution. Although franckeite exsolution in galena has not been reported previously, disk-shaped inclusions with topotaxial relations to the galena suggest that they are also products of exsolution. Both franckeite and diaphorite inclusions have topotaxial relations to galena, with coherent or semicoherent interfac-

es. These crystallographic relations result from the structural similarities between galena and the galena-derivative structures of diaphorite and the T layer in franckeite. The interfaces and orientations of exsolution features are a function of the misfit between the two phases and their elastic properties (Yund and Tullis, 1983, and references therein). Without knowledge of the elastic constants for diaphorite and franckeite, we can only consider the relations in terms of misfit.

Because the diaphorite substructure is only slightly smaller than the galena structure, the misfit at diaphorite-galena interfaces is relatively small and is accommodated by misfit dislocations. The interfacial strain is minimized by the rod morphology of the inclusions along **c**, the axis with the least misfit. The relatively $Ag_{0.5}Sb_{0.5}S$-rich galena from La Paz (1.37 mol%) probably experienced diaphorite exsolution at a higher temperature than the Zacatecas sample, which contains only 0.44 mol% $Ag_{0.5}Sb_{0.5}S$. As a result of higher Ag and Sb concentrations and temperatures, the La Paz sample contains coarser and more irregularly shaped diaphorite inclusions. Comparing rod lengths and widths in backscattered-electron images, an average aspect ratio for diaphorite rods in the La Paz galena is 16:1, whereas that determined for the Zacatecas galena is 47:1. The higher aspect ratios of Zacatecas diaphorite reflect the increased importance of interfacial strain energy during exsolution in the samples less rich in Ag and Sb.

The exsolution of diaphorite in both samples suggests that a solvus exists between galena and diaphorite in the PbS-$AgSbS_2$ system. However, experimental investigations of phase equilibria in the PbS-$AgSbS_2$-Sb_2S_3 system above 300 °C (Hoda and Chang, 1975; Amcoff, 1976) indicate a solvus between galena and freieslebenite ($AgPbSbS_3$). One explanation is that equilibrium was not attained in the experimental studies and that freieslebenite exsolved metastably. This seems unlikely because both studies found immiscibility between galena and freieslebenite in PbS-rich samples, and Hoda and Chang (1975) found a second miscibility gap between diaphorite and freieslebenite. A second explanation for the occurrence of diaphorite in galena is that it exsolves metastably because of a coherent solvus at lower temperatures than the freieslebenite-galena solvus. This explanation is possible if diaphorite meshes with the galena structure more easily than freieslebenite. A comparison of the misfit values for diaphorite and freieslebenite (Table 2) indicates that the strain is more evenly distributed along **a** and **b** for diaphorite-galena intergrowths. Although the misfit differences appear small, they are apparently large enough to reduce the nucleation energy for diaphorite relative to freieslebenite in some Ag-Sb-bearing galena.

Acknowledgments

We thank Donald Burt and Julio Pinto for the La Paz sample, Michael Sheridan for the Zacatecas sample, and Louis Cabri for the synthetic Ag-bearing samples. We also thank Nancy Brown, Gerry Czamanske, and Tamsin McCormick for helpful reviews of the manuscript, as well as Su Wang for discussions concerning franckeite structure and James Clark for assistance with the electron microprobe. This work was funded by NSF grant EAR-8708529. The electron microprobe facility is funded by NSF grant EAR-8408529 and the HRTEM at Arizona State University is funded by the NSF and ASU.

References cited

Amcoff, O. (1976) The solubility of silver and antimony in galena. Neues Jahrbuch für Mineralogie Monatshefte, 6, 247–261.

Bakken, B.M., Hochella, M.F., Marshall, A.F., and Turner, A.M. (1989) High-resolution microscopy of gold in unoxidized ore from the Carlin mine, Nevada. Economic Geology, 84,171–179.

Cabri, L.J. (1987) The mineralogy of precious metals: New developments and metallurgical implications. Canadian Mineralogist, 25,1–7.

——— (1992) The distribution of trace precious metals in minerals and mineral products: The 23rd Hallimond Lecture (1991). Mineralogical Magazine, 56, 289–308.

Cabri, L.J., Harris, D.C., and Nobling, R. (1984) Trace silver analysis by proton microprobe in ore evaluation. In U. Kudryk, D.A. Corrigan, and W.W. Liang, Eds., Precious metals: Mining, extraction, and processing. Metallurgical Society of AIME Proceedings, p. 93–100. Warrendale, Pennsylvania.

Cabri, L.J., Campbell, J.L., Laflamme, J.H.G., Leigh, R.G., Maxwell, J.A., and Scott, J.D. (1985) Proton-microprobe analysis of trace elements in sulfides from some massive sulfide deposits. Canadian Mineralogist, 23, 133–148.

Cabri, L.J., Chryssoulis, S.L., De Villiers, J.P.R., Laflamme, J.H.G., and Buseck, P.R. (1989) The nature of "invisible" gold in arsenopyrite. Canadian Mineralogist, 27, 353–362.

Cabri, L.J., Chryssoulis, S.L., Campbell, J.L., and Teasdale, W.J. (1991) Comparison of in-situ gold analyses in arsenian pyrite. Applied Geochemistry, 6, 225–230.

Chryssoulis, S.L., and Cabri, L.J. (1990) Significance of gold mineral balances in mineral processes. Transactions of the Institution of Mining and Metallurgy, Section C99, C1–C10.

Chryssoulis, S.L., Chauvin, W.J., and Surges, L.J. (1986) Trace element analysis by secondary ion mass spectrometry with particular reference to silver in Brunswick sphalerite. Canadian Metallurgical Quarterly, 25, 233–239.

Czamanske, G.K., and Hall, W.E. (1976) The Ag-Bi-Pb-Sb-S-Se-Te mineralogy of the Darwin lead-silver-zinc deposit, southern California. Economic Geology, 70, 1092–1110.

Foord, E.E., Shawe, D.R., and Concklin, N.M. (1988) Coexisting galena, PbS and sulfosalts: Evidence for multiple episodes of mineralization in the Round Mountain and Manhattan gold districts, Nevada. Canadian Mineralogist, 26, 355–376.

Godovikov, A.A., and Nenasheva, S.N. (1969) The $AgSbS_2$-PbS system above 480° C. Døkilady Academie Nauk SSSR, 185, 76–79.

Hellner, E.V. (1957a) Über komplex zusammengesetzte Spie Glanze. III. Zur Struktur des Diaphorite $Pb_2Ag_3Sb_3S_8$. Zeitschrift für Kristallographie, 110, 169–174.

——— (1957b) Über komplex zusammengesetzte Erze. II. Zur Structur des Freieslebenite $PbAgSbS_3$. Zeitschrift für Kristallographie, 109, 284–295.

Hoda, S.N., and Chang, L.L.Y. (1975) Phase relations in the systems PbS-AgS_2-Sb_2S_3 and PbS-AgS_2-Bi_2S_3. American Mineralogist, 60, 621–633.

Karup-Møller, S. (1977) Mineralogy of some Ag-(Cu)-Pb-Bi sulfide associations. Bulletin of the Geological Society of Denmark, 26, 41–68.

Laflamme, J.H.G., and Cabri, L.J. (1986a) Silver and antimony contents of galena from the Brunswick No. 12 mine. CANMET Mineral Sciences Laboratories Division Report MSL, 86–138, p. 1–13.

——— (1986b) Silver and bismuth contents of galena from the Brunswick No. 12 mine. Project 30.77.01: Silver recovery in the zinc industry. CANMET Mineral Sciences Laboratories Division Report MSL, 86–91, p. 1–16.

Makovicky, E. (1974) Mineralogical data on cylindrite and incaite. Neues Jahrbuch für Mineralogie Monatshefte, 6, 235–256.

——— (1976) Crystallography of cylindrite. Part I. Crystal lattices of cylindrite and incaite. Neues Jahrbuch für Mineralogie Abhandlungen, 126, 304–326.

McIntyre, N.S., Cabri, L.J., Chauvn, W.J., and Laflamme, J.H.G. (1984) Secondary ion mass spectrometry study of dissolved silver and indium in sulfide minerals. Scanning Electron Microscopy, 3, 1139–1147.

Moh, G.H. (1984) Sulfosalts: Observations and mineral descriptions, experiments and applications. Neues Jahrbuch für Mineralogie Abhandlungen, 150, 25–64.

——— (1987) Current ore petrography: Microscopy, genesis, analysis, and experimentation. Neues Jahrbuch für Mineralogie Abhandlungen, 153, 245–324.

Ramdohr, P. (1980) The ore minerals and their intergrowths. In International series in earth sciences, vol. 35 (2nd edition), 1207 p. Pergamon, New York.

Shannon, R.D. (1976) Revised effective ionic radii and systematic studies of interatomic distances in halides and chalcogenides. Acta Crystallographica, A32, 751–767.

Sharp, T.G., and Buseck, P.R. (1989) Distribution of silver in galena: A high spatial resolution study. Geological Society of America Abstracts with Programs, 21-6, A248.

Sharp, T.G., Zheng, N.J., Tsong, I.S.T., and Buseck, P.R. (1990) Scanning tunneling microscopy of defects in Ag- and Sb-bearing galena. American Mineralogist, 75, 1438–1442.

Van Hook, H.J.K (1960) The ternary system Ag_2S-Bi_2S_3-PbS. Economic Geology, 55, 759–787.

Wang, S., and Kuo, K.H. (1991) Crystal lattices and crystal chemistry of cylindrite and franckeite. Acta Crystallographica, 47A, 381–392.

Wernick, J.H. (1960) Constitution of the $AgBiS_2$-$AgBiSe_2$ systems. American Mineralogist, 45, 591–598.

Williams, T.B., and Hyde, B.G. (1988) Electron microscopy of cylindrite and franckeite. Physics and Chemistry of Minerals, 15, 521–544.

Wycoff, R.W.G. (1963) Crystal structures I. 467 p. Wiley, New York.

Yund, R.A., and Tullis, J. (1983) Subsolidus phase relations in the alkali feldspars with emphasis on coherent phases. In Mineralogical Society of America Reviews in Mineralogy, 2, 141–176.

Manuscript received November 1, 1991
Manuscript accepted August 24, 1992